3-D Crustal Shear Wave Velocity Model Derived from the Adjoint Waveform Tomography in the Central Japan Island

Kota Mukumoto[1,1,1] and Takeshi Tsuji[1,1,1]

[1]Kyushu University

November 30, 2022

Abstract

Adjoint waveform tomography, which is an emerging seismic imaging method for the crust- and global-scale problems, has gained popularity in the past and present decade. This study, for first time, applies adjoint waveform tomography to the large volume of seismic data recorded by the densely spaced, permanent monitoring network that covers the entirety of Japan. We develop a heterogeneous shear-wave velocity model of central Japan that agrees with the geology and lithology. The results reduce the time-frequency phase misfit by 16.4% in the 0.02–0.05 Hz frequency band and 6.7% in the 0.033–0.1 Hz band, respectively. We infer that some velocity anomalies resolved in this work would reflect the subsurface structures such as the volcanic fluids, dehydration of the subducted crust, and sedimentary basin. In addition, dense distributions of deep earthquakes are visible beneath the high-velocity blocks estimated in this study. The results of this study suggest the possibility of imaging large scale heterogeneous subsurface structures using waveform tomography with a densely distributed network of permanent seismometers.

submitted to Geophys. J. Int.

3-D Crustal Shear Wave Velocity Model Derived from the Adjoint Waveform Tomography in the Central Japan Island

Kota Mukumoto[1], Takeshi Tsuji[1,2,3]

[1] Department of Earth Resources Engineering, Kyushu University, Fukuoka, Japan

[2] Faculty of Engineering, The University of Tokyo, Tokyo, Japan

[3] International Institute for Carbon-Neutral Energy Research (I2CNER), Kyushu University, Fukuoka,Japan

8 June 2022

SUMMARY

Adjoint waveform tomography, which is an emerging seismic imaging method for the crust- and global-scale problems, has gained popularity in the past and present decade. This study, for first time, applies adjoint waveform tomography to the large volume of seismic data recorded by the densely spaced, permanent monitoring network that covers the entirety of Japan. We develop a heterogeneous shear-wave velocity model of central Japan that agrees with the geology and lithology. The results reduce the time-frequency phase misfit by 16.4% in the 0.02–0.05 Hz frequency band and 6.7% in the 0.033–0.1 Hz band, respectively. We infer that some velocity anomalies resolved in this work would reflect the subsurface structures such as the volcanic fluids, dehydration of the subducted crust, and sedimentary basin. In addition, dense distributions of deep earthquakes are visible beneath the high-velocity blocks estimated in this study. The results of this study suggest the possibility of imaging large scale heterogeneous subsurface structures using waveform tomography with a densely distributed network of permanent seismometers.

Key words: Crustal structure, Crustal imaging, Waveform inversion, Seismic tomography in Japan

1 INTRODUCTION

The island nation of Japan is located on the convergent boundary where the Philippine Sea plate and the Pacific plate are subducting beneath the Eurasian and the Okhotsk plates. The interactions of these four main plates are responsible for many of Japan's unique tectonic features (Figure 1). The boundary between the Pacific and Eurasian plates on land is the Itoigawa– Shizuoka tectonic line (ISTL), which extends from Itoigawa city in Niigata prefecture to Shizuoka city in Shizuoka prefecture. The subduction of the Philippine Sea Plate created the Izu–Bonin (arc–arc) collision zone (IBCZ), where the Izu–Bonin arc has collided with the Honshu arc. The area also includes two prominent structural features: the Median tectonic line (MTL) and the Niigata–Kobe tectonic line (NKTL). Central Japan contains many active volcanoes, sedimentary basins, the IBCZ, and several major tectonic lines (ISTL, MTL, and NKTL). Therefore, the seismic structure of the region is expected to contain substantial lateral heterogeneities. The complex geological structures of central Japan have been the subject of many previous geophysical studies, which have relied mainly on regional- and exploration-scale seismic tomography (Arai et al., 2013; Arai & Iwasaki, 2014; Nakajima & Hasegawa, 2007a, 2007b; Nakajima et al., 2009; Hirose et al., 2008; Nishida et al., 2008; Nimiya et al., 2020; Miyoshi et al., 2017). For example, a series of studies using first-arrival tomography (Nakajima & Hasegawa, 2007a, 2007b; Nakajima et al., 2009) revealed the slab geometry of the Philippine Sea Plate and investigated plausible relationships between the arc magmatism and the subducting oceanic plates. Nishida et al. (2008) and Nimiya et al. (2020) leveraged the ambient noise wavefield using seismic interference and clearly imaged underground structures including magmatic fluids and thick sedimentary successions. Recently, the development of adjoint waveform tomography techniques has improved our ability to resolve subsurface structures (Fichtner et al., 2009, 2010; Tape et al., 2010; Simutė et al., 2016; Lei et al., 2020). In this method, three-dimensional (3D) sensitivity distributions of seismic waves can be computed by full numerical seismic wave simulation in heterogeneous media using the adjoint method (Tarantola, 1984; Mora, 1987; Tromp et al., 2005; Fichtner, 2010). Furthermore, first-arrival tomography and ambient noise tomography use specific seismic phases, whereas adjoint waveform tomography can use as much waveform information as possible without requiring selections of seismic phases. Miyoshi et al. (2017) firstly applied adjoint tomography using broad band seismic stations of F-net in Kanto area and obtained stronger heterogeneous velocity model compared to the one estimated using ray-tomography. Therefore, the application of adjoint waveform tomography might improve tomographic imaging of heterogeneous seismic velocity structures beneath central Japan.

The goals of the present work are to resolve crustal S-wave velocity structures in central Japan based on adjoint waveform tomography, and to investigate whether it is possible to obtain detailed tomographic images comparable to those resolved by other popular methods (e.g., first-arrival or ambient noise tomography). Here, we apply adjoint waveform tomography to the large volume of seismic data collected by Hi-net and F-net (Okada et al., 2004). The estimated crustal S-wave velocity model reaches a minimum misfit after 17 iterations and shows strong lateral velocity variations. The velocity anomalies in the estimated model are in good agreement with the geology.

2 METHOD

2.1 3D seismic wave simulation and initial model

Synthetic waveforms of 240 sec were calculated using the spectral element method, which is widely used in seismology due to its accuracy and ease of code parallelisation (Komatitsch & Tromp, 1999, 2002). We used the program SPECFEM3D Cartesian for forward and adjoint 3D isotropic seismic wave simulations (Peter et al., 2011). We calculated seismic wavefields in our target model volume of 133.5°–140.5° in longitude × 32.5°–37.5° in latitude × 0–90 *km* in depth with mesh accurate up to seismic wave of 2.5 *sec* period. The laterally homogeneous seismic velocity model named JMA2001 was used as the initial model (Ueno et al., 2002); this provides S- and P- wave velocity structures around Japan. We obtained initial density structures using empirical relationship between P-wave velocity and density

(Brocher, 2005):

$$\rho = 1.6612V_p - 0.4721V_p^2 + 0.0671V_p^3 - 0.0043V_p^4 + 0.000106V_p^5, \quad (1)$$

where ρ is in g/cm^3 and V_p is in km/sec.

2.2 Computation of misfit function

Noisy observed data, which is dissimilar to synthetic data, could result in incorrect model parameters. In addition, cycle skipping can lead to a local minimum in the waveform inversion's solution space that does not correspond to true structure. The latter phenomenon can occur when observed waveforms are more than half a wavelength out of phase from synthetic waveforms; therefore, data selection must be carried out as carefully as possible to prevent this. In this study, we automatically determine the time-windows of pairs of synthetic and observed waveforms based on parameters such as time lag, the cross-correlation coefficient between observed and synthetic waveforms, and the signal-to-noise ratio, using the program FLEXWIN (Maggi et al., 2009). We optimized the model parameters in two frequency ranges: 0.02–0.05 and 0.0333–0.1 Hz, and time-window selection was carried out before the first iteration for each frequency range. We set the maximum time lag between observed and synthetic waveforms to 12 *sec* during selections of time-windows for 0.02–0.05 Hz and 5 *sec* for 0.033–0.1 Hz. As a result, time-windows were determined for 2,860 waveform pairs in 0.02–0.5 Hz and 15,523 in 0.033-0.1 Hz. The quantification of the misfit between synthetic and observed data was based on phase misfit using the time-frequency transform (Fichtner et al., 2008, 2009):

$$E_p^2(u_i^0, u_i) = \iint W_p^2(t,\omega)W_t(t)^2[\phi_i(t,\omega) - \phi_i^0(t,\omega)]^2 dtd\omega, \quad (2)$$

where u_i^0 and u_i are ith component observed and synthetic velocity data, ϕ_i^0 and ϕ_i are time-frequency phase of observed and synthetic velocity data, W_t is time window selected by FLEXWIN and W_p is weighting function. The weighting function in this study was chosen by following Fichtner et al (2008):

$$W_p = log(1 + |\tilde{u}|)/\max_{t,\omega} \log(1 + |\tilde{u}|), \tag{3}$$

where $\tilde{u}$ is the velocity data on the time-frequency plane.

2.3 Model update

We used a multiscale strategy that first recovers the smooth structures, then resolve finer-scale structures by broadening the frequency range (from 0.02–0.05 to 0.033–0.1 Hz). The most energetic phase in our data is the surface wave; therefore, only the S-wave velocity was updated between iterations.

We computed gradient of misfit function with respect to model parameter using the adjoint method, then updated model in the scheme of Newton's method. Approximate inverse hessian kernels were applied to gradients of each event. This inverse hessian kernel acts as a preconditioner in Newton's method (Tape et al., 2010). Model update at $i + 1$th iteration in this study is

$$m_{i+1} = m_i - \alpha S[\tilde{H}^{-1}(m_i)g(m_i)], \tag{4}$$

where m_i is current model parameter, α is step length which scales descent direction, $\tilde{H}(m)$ is approximate hessian, $g(m)$ is gradient of misfit function, and S is smoothing operator. Smoothing of the gradient was performed by convolution with a 3D Gaussian. Based on the bandwidth of the data and inspired by Chow et al. (2022), we set horizontal and vertical standard deviations of the 3D Gaussian to 20 and 10 km for 0.02–0.05 Hz, and 10 and 6 km for 0.033–0.1 Hz. Step length $\alpha_{x\%}$ was determined using following manner at each iteration to select enough small step length ($\alpha_{x\%}$ means that step length is set so that the change between current model m_i and updated model m_{i+1} is $< x\%$).

(i) Two total misfits using $\alpha_{x\%}$ and $\alpha_{x+1\%}$ were calculated before going to next iteration and adopted $\alpha_{x\%}$ if misfit of $\alpha_{x\%}$ is $> \alpha_{x+1\%}$.

(ii) Step length $\alpha_{x\%}$ is reduced to $\alpha_{x/2\%}$ if misfit of $\alpha_{x\%}$ is $< \alpha_{x+1\%}$.

(iii) Step length is increased to $\alpha_{2\times x\%}$ from $\alpha_{x\%}$ only if reductions of misfits compared to previous iteration are < 1 % over past 2 iterations.

We firstly employed $\alpha_{2\%}$ and changed step length at each iteration by following above manner. When misfit of updated model m_{i+1} is larger than one of current model m_i, we stopped inversion at ith iteration.

3 DATA

Earthquake waveform data were collected from the Hi-net high-sensitivity seismograph network and F-net broad-band seismograph network, operated across Japan by the National Research Institute for Earth Science and Disaster Prevention (NIED) (Okada et al., 2004). There are 388 Hi-net and 28 F-net permanent stations in our study area (Figure 2(a)), all have three-component velocity seismometers and are deployed in boreholes. We used F-net stations for the inversion of 0.02–0.05 and 0.033–0.1 Hz, while Hi-net stations were used only for 0.033–0.1 Hz. The seismometers of Hi-net are designed to have sensitivities >1.0 Hz; however, our target frequency range is 0.02–0.1 Hz. Therefore, we applied the sensitivity corrections proposed by Maeda et al. (2011) to enhance low-frequency component and used Hi-net data in the inversion only for higher frequency range 0.033–0.1 Hz.

We collected data from 41 earthquakes that occurred between 2004 and 2021 with moment magnitudes 4.4$\leq Mw \leq$5.5 and depths shallower than 60 km (Figures 2). We prepared inversion dataset and validation dataset. Inversion dataset includes 29 earthquakes data and was used for the inversion of S-wave velocity model, while validation dataset consisting 12 earthquakes was used for only the validation of resultant model. Earthquakes in the validation dataset were chosen so that their locations do not overlap with those in the inversion dataset (Figures 2(b) and 2(c)). Earthquake parameters for simulations were extracted from their Global CMT solutions (Ekström et al., 2012); these values were fixed while updating our velocity models, because inversion for source parameter updates requires additional computation time. In addition, we restricted the data to recordings at source–receiver distances of >80 km.

4 RESULTS AND INTERPRETATIONS

After 11 iterations of the 0.02–0.05 Hz band and 6 iterations of the 0.033–0.1 Hz band we obtained the S-wave velocity model shown in Figures 3. The S-wave velocity outside the dashed lines in Figures 3 cannot be accurately estimated due to the less sensitivity of our inversion dataset (discussed later). The results show strong horizontal velocity variations: for example, at 5 km depth, low-velocity anomalies reach <3000 m/s, whereas high-velocity anomalies are ∼4000 m/s. The misfit is reduced by 16.4% in the 0.02–0.05 Hz band and 6.7% in the 0.033–0.1 Hz band (Figure 4).

We confirmed that the misfits between observed and synthetic waveforms were improved after 17 iterations; representative examples are shown in figures 5. Not only phases but also amplitudes are improved after 17 iterations. However, unchanged waveforms between after and before inversion can be seen in horizontal components of panel D. This can be happened due to inappropriate earthquake source parameter or insufficient model parameterization (elastic isotropic parameterization in our study). Therefore, there is chance to improve our velocity model by including inversions of earthquake source parameters and elastic anisotropic parameters. This is a part of our future study.

The largest feature in the resultant S-wave velocity model at shallower depths $\leq 10\ km$ is that the northern part of the study area where active volcanoes exist is characterized by low velocities, whereas high velocities dominate in the south. This general finding agrees with previous studies (J. Nakajima & Hasegawa, 2007a; Nishida et al., 2008). At shallow depths, there is a distinct low-velocity anomaly around region A. The Niigata sedimentary basin, which formed during the opening of the Japan Sea (Takano, 2002), covers a portion of this low-velocity anomaly. In addition, multiple active volcanoes, such as Asama mountain and Kusatsu–Shirane mountain, are in this region. Therefore, the low-velocity anomaly could be due in part to the sedimentary basin as well as magmatic fluids associated with back-arc volcanism. The high-velocity anomalies aligned from southwest to northeast were imaged at depths $\leq 10\ km$ (B1–B3 in figures 3). These anomalies partially agree with previous model derived from ambient noise tomography (Nishida et al., 2008). Figures 6(a) and (b) show the S-wave velocity at 10 *km* with epicenters of shallow earthquakes (0–25 *km*) and deep earthquakes (25–50 *km*). The hypocenters of earthquakes shown in Figures 6(a) and (b) was taken from JUICE catalog (Yano et al., 2017). Correlation between high-velocity anomalies and shallow earthquakes are unclear, while there is dense distributions of deep earthquakes around high-velocity blocks B1–B3.

At deeper depths ≤ 25 *km*, four low-velocity anomalies appear in the south; regions C1, C2, D, and E. The boundary between the Philippine Sea Plate and the Eurasian Plate around C1, C2 and D is around 30 *km* depth (Hirose et al., 2008; J. Nakajima et al., 2009), thus, the dehydrated fluid from the hydrous minerals of the subducted oceanic crust would be one of the interpretations of lower seismic velocity. The region around IBCZ (between C1 and C2) is characterized by no lower S-wave velocity. Seno and Yamasaki (2003) hypothesized that there is no or less dehydration reactions in the subducted slab beneath the IBCZ. In addition, Arai et al. (2013) imaged the subsurface structure at IBCZ using active-seismic data and proposed that thick crust of Izu-Bonin arc above the oceanic crust result in less infiltration of seawater to oceanic crust. Based on these studies, we infer that absense of low velocity anomaly around IBCZ is caused by less dehydration due to the existence of thick crust of Izu-Bonin arc. Lower seismic velocities of region D is located beneath the chain of active volcanoes of Izu-Bonin arc and might be related with magmatic activities of active volcanoes.

Figure 6(c) shows the S-wave velocity at 25 *km* depth with distributions of low-frequency earthquakes (LFEs) estimated by Kato et al. (2020). Nakajima and Hasegawa. (2016) revealed that P-wave velocity above the subducted plate is low above places where activities of LFEs are less, however velocity is normal above places where there is activities of LFEs (Ise gaps and Tokai region in Figure 6 (c)). Therefore, the existence of lower S-wave velocity at region D, C1, and C2 is well consistent with observations of their study.

5 DISCUSSION

We conducted resolution analysis using point spread functions (PSFs) to assess the tomographic inversions of this study. PSFs are point-localized perturbations from background models. Estimating the response of a tomographic inversion to PSFs allows to evaluate how much blur and smear are generated (Fichtner and Trampert, 2011). In this study, we computed Hessian on a model perturbation using approximated equation

$$H(m)\delta m \approx g(m + \delta m), \tag{5}$$

where H(m) denotes the Hessian at the final model m, δm is perturbations and $g(m + \delta m)$ is the gradient of perturbated model. We computed responses $H\delta m$ for lower frequency range 0.02–0.05 Hz only and applied smoothing using 3D Gaussian with same deviations in our velocity inversion. Figures 7 show the results of individual PSFs tests for some interest velocity anomalies B1–B3, C1, C2, and D in our velocity model. We put 3D Gaussian functions with horizontal and vertical standard deviations of 15 and 6 km as a δm. Localized δm is located at 7 km depth and has -15% peak perturbation for high-velocity anomalies B1–B3, while δm is located at 25 km depth with +15% peak perturbations for low-velocity anomalies C1, C2, and D. The results of PSFs tests for B2 and B3 (Figures 7(b) and (c)) show that peaks of $H\delta m$ are well coincide with the locations of velocity perturbations and support the existence of high-velocity anomalies at B2 and B3. However, large vertical smearing can be seen in the result of PSF test for B1 (Figure 7(a)). This suggests that actual termination of high-velocity zone of B1 extending to 35 km depth seems to be shallower than our velocity model. Velocity perturbations are accurately mapped to $H\delta m$ in the results of PSFs tests for C1, C2 and D although the peaks are slightly shifted (Figures 7(d), (e) and (f)). There is no large smearing like result for B1 and we conclude that detected low-velocity anomalies C1, C2 and D accurately reflect the existence of dehydrated fluids around 25 km depth.

To investigate how much our configurations of inversion such as limited frequency bands and source-station pairs have a sensitivity to target model volume, we computed $H\delta m$ by replacing δm of PSFs test with 50 m/s of constant volumetric velocity perturbation. The

Hessian respected to volumetric constant velocity perturbation corresponds to the zero-wavenumber component of Hessian in frequency-wavenumber domain (Fichtner and Trampert, 2011). Figures 8 show the normalized response to the constant volumetric velocity perturbation at each frequency band. As expected, $H\delta m$ of lower frequency band has large values at greater depth compared to the one of higher frequency band. The largest values of $H\delta m$ are shallower than 40 km depth and no or very low sensitivity at depth $\leq$ 60 km. Therefore, 90 km depth of our model volume is enough deep to compute seismic waves included in our data set. We set 0.2 of threshold value to exclude regions where sensitivity is not enough high from our interpretations of velocity models (dashed lines in Figures 3, 6, and 8).

Validation dataset (Figure 2(c)) which was not included in inversion offer additional information about results of inversion. If there is no or less misfit reduction of validation data set, solutions of inversion could be overestimated. To estimate not only time-frequency phase misfit but also other measurements, we employs normalized waveform difference misfit

$$E^2(m) = \frac{\int [u^{obs}(t) - u(t,m)]^2 dt}{\sqrt{\int u^{obs}(t)^2 dt \int u(t,m)^2 dt}} \tag{6}$$

used in previous studies, for example, Tape et al. (2010) and Simute et al. (2016). $u^{obs}(t)$ and $u(t,m)$ in equation (6) are observed and synthetic data. We used validation dataset in frequency range 0.033–0.1 Hz, not in entire frequency range 0.02–0.1 Hz to include Hi-net data in validation dataset. The validation dataset was selected by FLEXWIN as well as the inversion dataset, however, we didn't employ any time-windows for the measure of normalized waveform difference misfit. Figure 9 shows the histograms of normalized waveform difference of initial and final model for validation dataset. Improvement of misfit in validation dataset suggests our inversion estimated meaningful velocity structures.

6 CONCLUSIONS

From seismic waveforms of 29 earthquakes recorded by 388 Hi-net and 28 F-net seismic stations we built a 3D S-wave velocity model using adjoint waveform tomography. The model estimation procedure was designed to minimize the time-frequency phase misfit between observed and synthetic seismic waveforms in the frequency bands 0.02–0.05 and 0.033–0.1 Hz. The final model resolves strong horizontal heterogeneities, with velocity values in the range 2800–4000 m/s. The low-velocity anomalies resolved in the present work appear to correspond to a thick sedimentary basin, volcanic fluids, and fluids related to dehydration of subducted plate. We imaged clearly three high velocity blocks at shallow depths ≤ 10 km, and there is intense seismicity beneath these high velocity blocks. Based on PSFs test, our dataset has enough sensitivity at regions of detected low- and high-velocity anomalies. In addition, the improved fit between observed and calculated waveforms obtained with our final model and evaluation using additional dataset which was not included in inversion support the accuracy of the results. This study confirms that adjoint waveform tomography and mixed dataset of F-net stations and densely distributed Hi-net stations in Japan can resolve S-wave velocity structure and explain known geology, yielding results comparable to other velocity models and seismic waveforms similar to observed data. Although we have not yet confirmed that earthquake data recorded by F-net and Hi-net stations have sufficient resolution for other regions characterized by complex geologic features, such as Kyushu and Hokkaido, the combination of adjoint waveform tomography, F-net and Hi-net station data will lead to accurate velocity models throughout the Japanese islands.

7 ACKNOWLEDGMENTS

This work was supported by the Japan Society for the Promotion of Sciencce (JSPS) through a Grant-in-Aid for JSPS Research Fellow (JP21J21871). We used the open-source software SPECFEM3D Cartesian for seismic wave simulation and we thank the developers of SPECFEM3D. We also thank the National Research Institute for Earth Science and Disaster Prevention (NIED) for providing us with Hi-net data. Seismic wave simulations were conducted on the ITO supercomputer system at the Research Institute for Information Technology, Kyushu University. We used the open-source software GMT (Generic Mapping Tools)(Wessel et al., 2013) to construct figures.

8 DATA AVAILABILITY

The Hi-net data is available from https://hinetwww11.bosai.go.jp/auth/?LANG=en. The CMT solutions used in this study are available from https://www.globalcmt.org/. The S-wave velocity model we built is avail-able at https://doi.org/10.6084/m9.figshare.20024279.

REFERENCES

Arai, R., Iwasaki, T., Sato, H., Abe, S., & Hirata,N., 2013. Crustal structure of the izu collision zone in central japan from seismic refraction data. Journal of Geophysical Research: Solid Earth 118(12), 6258–6268.

Arai, R., & Iwasaki, T., 2014. Crustal structure in the northwestern part of the izu collision zone in central japan. Earth, Planets and Space 66(1), 1–12.

Brocher, T. M., 2005. Empirical relations between elastic wave speeds and density in the earth's crust. Bulletin of the seismological Society of America 95(6),2081–2092.

Chow, B., Kaneko, Y., Tape, C., Modrak, R., Mortimer, N., Bannister, Stephen., & Townend, J., 2022. Strong Upper-Plate Heterogeneity at the Hikurangi Subduction Margin (North Island, New Zealand) Imaged by Adjoint Tomography. Journal of Geophysical Research: Solid Earth 127, e2021JB022865.

Ekström, G., Nettles, M., & Dziewo ński, A. M., 2012. The global cmt project2004–2010: Centroid-moment tensors for 13,017 earthquakes. Physics of theEarth and Planetary Interiors 200, 1–9.

Fichtner, A., Kennett, B. L. N., Igel, H., & Bunge, H. P., 2008. Theoretical background for continental-and global-scale full-waveform inversion in the time–frequency domain. Geophysical Journal International 175(2), 665–685.

Fichtner, A., Kennett, B. L. N., Igel, H., & Bunge, H. P., 2009. Full seismic waveform tomography for upper-mantle structure in the australasian region using adjoint methods. Geophysical Journal International 179(3), 1703–1725.

Fichtner, A., 2010. Full seismic waveform modelling and inversion. Springer Sci-ence & Business Media.

Fichtner, A., Kennett, B. L. N., Igel, H., & Bunge, H. P., 2010. Full waveform tomography for radially anisotropic structure: new insights into present and past states of the australasian upper mantle. Earth and Planetary Science Letters 290(3-4), 270–280.

Fichtner, A., & Trampert, J., 2011. Resolution analysis in full waveform inversion. Geophysical Journal International 187(3), 1604–1624.

Hirose, F., Nakajima J., & Hasegawa, A., 2008. Three-dimensional seismic velocity structure and configuration of the Philippine Sea slab in southwestern Japan estimated by double-difference tomography. Geophysical Research: Solid Earth 113(B9).

Kato, A., & Nakagawa, S., 2020. Detection of deep low-frequency earthquakes in the Nankai subduction zone over 11 years using a matched filter technique. Earth Planets Space 72, 128.

Komatitsch, D., & Tromp, J., 1999. Introduction to the spectral element method for three-dimensional seismic wave propagation. Geophysical journal international 139(3), 806–822.

Komatitsch, D., & Tromp, J., 2002. Spectral-element simulations of global seismic wave propagation—i. validation. Geophysical Journal International 149(2),390–412.

Lei, W., Ruan, Y., Bozdağ, E., Peter, D., Lefebvre, M., Komatitsch, D., Tromp, J., Hill, J., Podhorszki, N., & Pugmire, D., 2020. Global adjoint tomography model glad-m25. Geophysical Journal International 223(1), 1–21.

Maeda, T., Obara, K., Furumura, T., & Saito, T., 2011. Interference of long-period seismic wavefield observed by the dense hi-net array in japan. Journal of Geophysical Research: Solid Earth 116(B10).

Maggi, A., Tape, C., Chen, M., Chao, D., & Tromp, J., 2009. An automated time-window selection algorithm for seismic tomography. Geophysical Journal Inter-national 178(1), 257–281.

Miyoshi, T., Obayashi, M., Peter, D., Tono, Y., & Tsuboi, S., 2017. Adjoint tomography of the crust and upper mantle structure beneath the kanto region using broadband seismograms. Progress in Earth and Planetary Science 4(1), 1–20.

Mora, P., 1987. Nonlinear two-dimensional elastic inversion of multioffset seismic data. Geophysics 52, 1211–1228.

Nakajima, J., & Hasegawa, A., 2007a. Deep crustal structure along the niigata-kobe tectonic zone, japan: Its origin and segmentation. Earth, planets and space 59(2), e5–e8.

Nakajima, J., & Hasegawa,A., 2007b. Subduction of the philippine sea plate beneath southwestern japan: Slab geometry and its relationship to arc magmatism. Journal of Geophysical Research: Solid Earth 112(B8).

Nakajima, J., Hirose, F., & Hasegawa, A., 2009. Seismotectonics beneath the tokyo metropolitan area, japan: Effect of slab-slab contact and overlap on seismicity. Journal of Geophysical Research: Solid Earth 114(B8).

Nakajima, J., & Hasegawa, A., 2016. Tremor activity inhibited by well-drained conditions above a megathrust. Nat Commun 7(1), 13863.

Nimiya, H., Ikeda, T., & Tsuji, T., 2020. Three-dimensional s wave velocity structure of central japan estimated by surface-wave tomography using ambient noise. Journal of Geophysical Research: Solid Earth 125(4), e2019JB019043.

Nishida, K., Kawakatsu, H., & Obara, K., 2008. Three-dimensional crustal s wave velocity structure in japan using microseismic data recorded by hi-net tiltmeters. Journal of Geophysical Research: Solid Earth 113(B10).

Okada, Y., Kasahara, K., Hori, S., Obara, K., Sekiguchi, S., Fujiwara, H., & Yamamoto, A., 2004. Recent progress of seismic observation networks in japan-hi-net, f-net, k-net and kik-net-. Earth, Planets and Space 56(8), xv–xxviii.

Peter, D., Komatitsch, D., Luo, Y., Martin, R., Goff, N. L., Casarotti, E., Loher, P. L., Magnoni, F., Liu, Q., Blitz, C., Nissen-Meyer, T., Basini, P., & Tromp, J., 2011. Forward and adjoint simulations of seismic wave propagation on fully unstructured hexahedral meshes. Geophysical Journal International 186(2), 721–739.

Seno, T., & Yamasaki, T., 2003. Low-frequency tremors, intraslab and interplate earthquakes in southwest Japan: From a view point of slab dehydration. Geophys. Res. Lett 30, 2171.

Simutė, S., Steptoe, H., Cobden, L., Gokhberg, A., & Fichtner, A., 2016. Full-waveform inversion of the japanese islands region. Journal of Geophysical Research: Solid Earth 121(5),3722-3741.

Takano, O., 2002. Changes in depositional systems and sequences in response to basin evolution in a rifted and inverted basin: an example from the neogeneniigata-shin'etsu basin, northern fossa magna, central japan. Sedimentary Geology 152(1-2), 79–97.

Tarantola, A., 1984. Inversion of seismic reflection data in the acoustic approximation. Geophysics 49, 1259–1266.

Tape, C., Liu, Q., Maggi, A., & Tromp, J., 2010. Seismic tomography of the southern california crust based on spectral-element and adjoint methods. Geophysical Journal International 180(1), 433–462.

Tromp, J., Tape, C., & Liu, Q., 2005. Seismic tomography, adjoint methods, time reversal and banana-doughnut kernels. Geophysical Journal International 160.1, 195-216.

Ueno, H., Hatakeyama, S., Aketagawa, T., Funasaki, J., & Hamada, N., 2002. Improvement of hypocenter determination procedures in the japan meteorological agency (in japanese). Q. J. Seismol 65, 123–134.

Wessel, P., Smith, W., Scharroo, R., Luis, J., & Wobbe, F., 2013. Generic mapping tools: improved version released. Eos, Transactions American Geophysical Union 94(45), 409–410.

Yano, T. E., Takeda, T., Matsubara, M., & Shiomi, K., 2017. Japan unified high-resolution relocated catalog for earthquakes (juice): crustal seismicity beneath the Japanese Islands. Tectonophysics 702, 19–28.

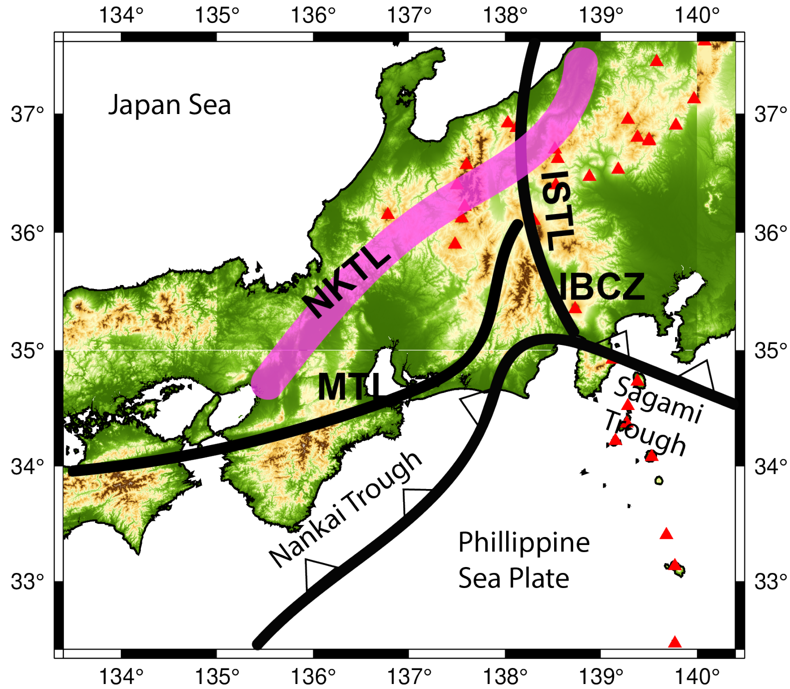

Figure 1: Map of study area. Black lines and pink area indicate major tectonic lines of Itoigawa-Shizuoka tectonic line (ISTL), Median tectonic line (MTL), and Niigata-Kobe tectonic line (NKTL). Red triangle indicate locations of active volcanoes.

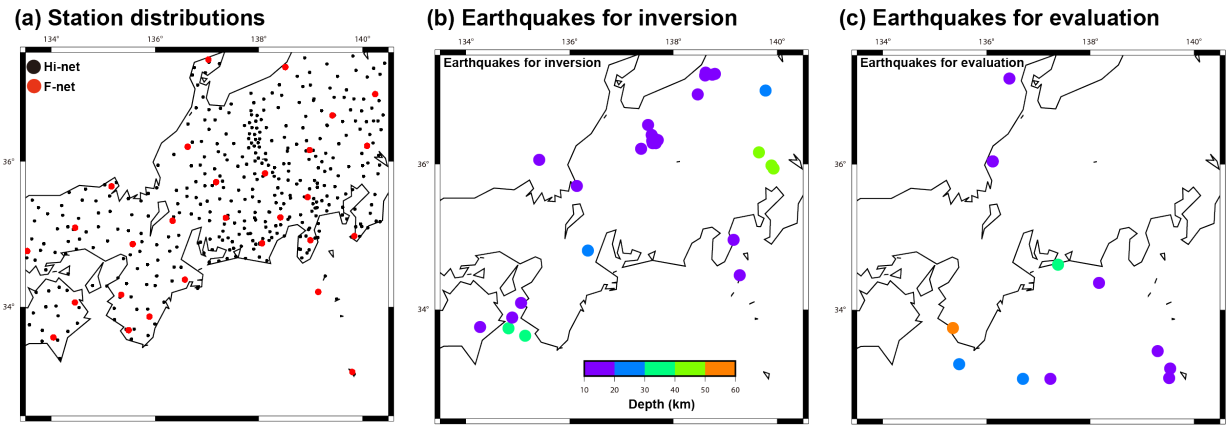

Figure 2: Data. (a)The distributions of Hi-net and F-net stations. (b)Epicenters of earthquakes for inversion. (c)Epicenters of earthquakes for validation.

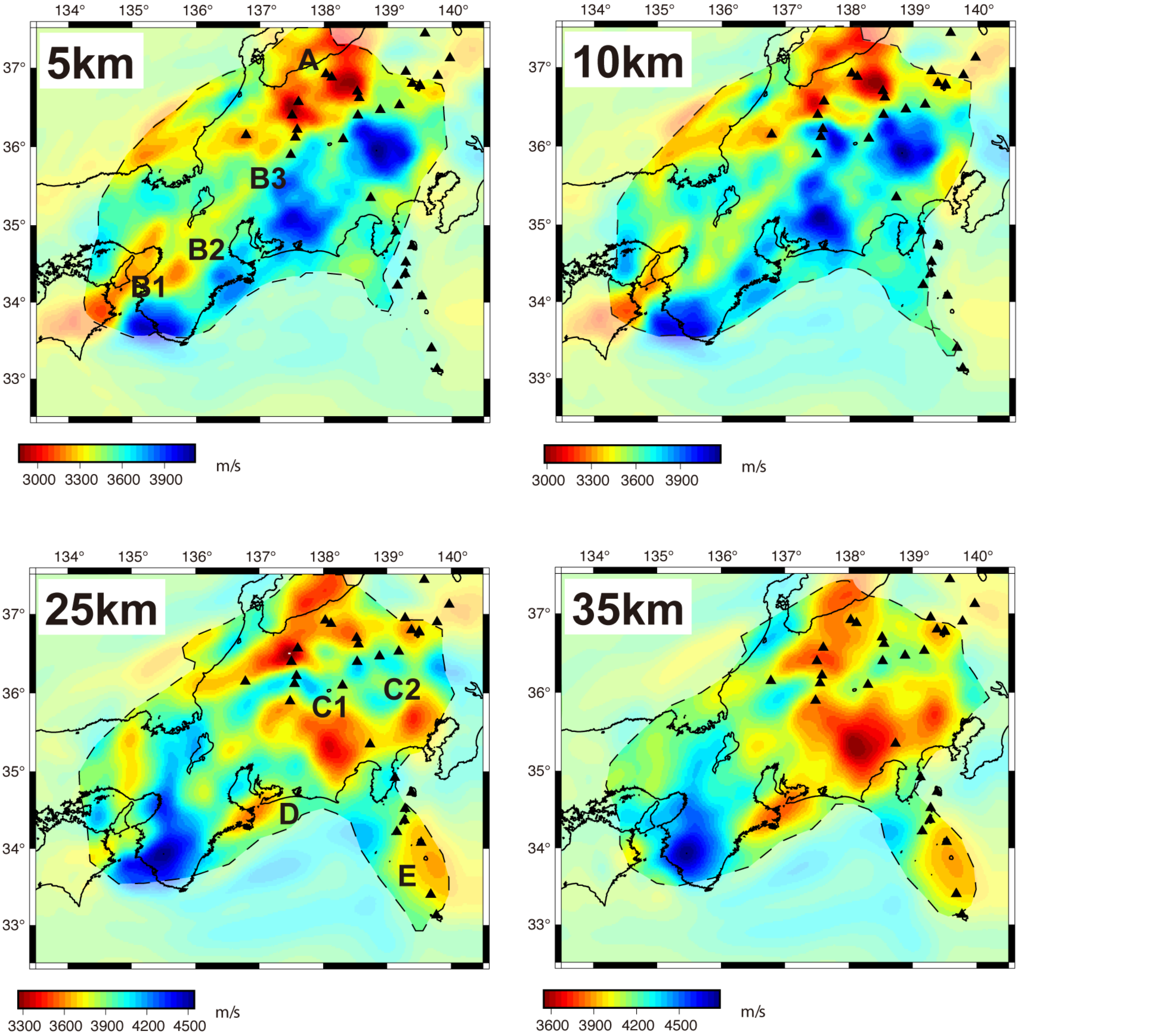

Figure 3: Resultant S-wave Velocity model sliced at depths of 5, 10, 25 and 35 km. The region enclosed by black dashed line is interpretable area explained in section 5. Black triangles show the locations of active volcanoes.

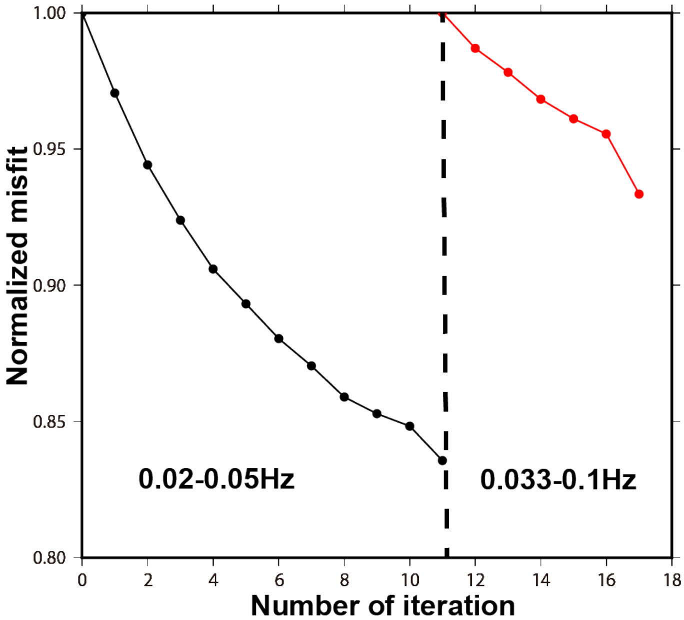

Figure 4: Misfit reduction. Normalized misfit reductions in the frequency ranges 0.02–0.05 and 0.033–0.1 Hz, respectively.

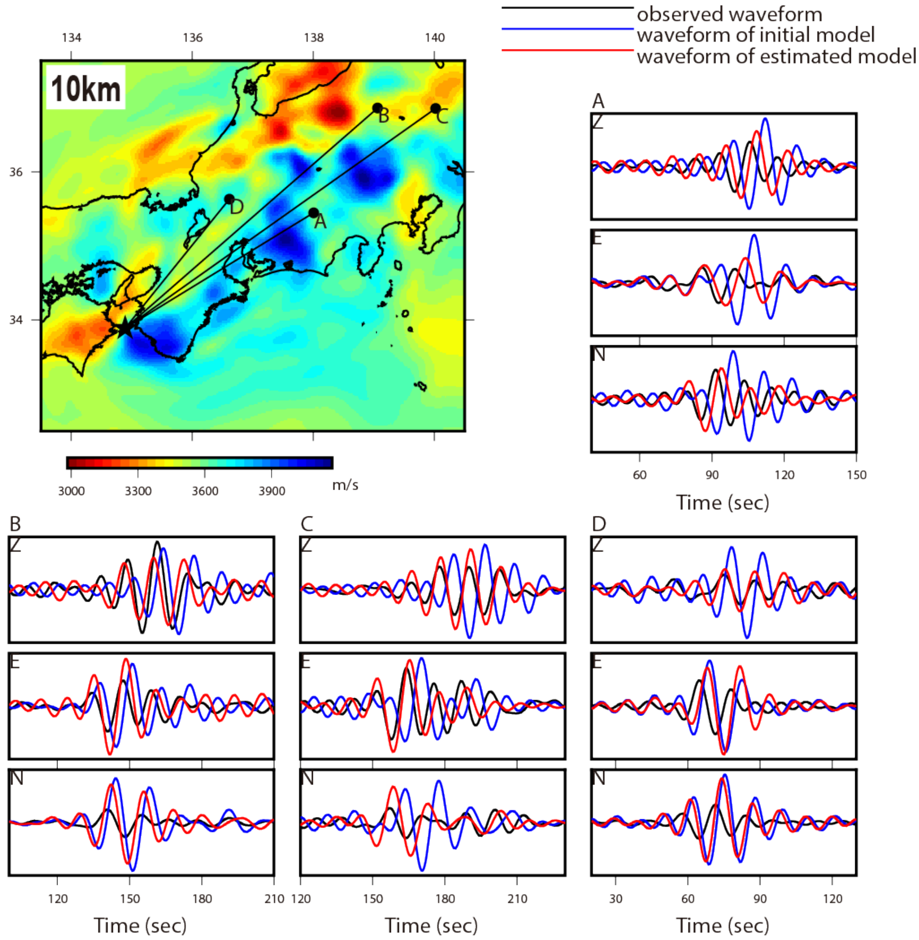

317

Figure 5: The improvement of waveform fittings. The upper-left subfigure shows S-wave velocity model at 10 km depth. The black star and circles indicate the epicenters and seismometers, respectively. Panels A–D show observed waveforms (black lines), waveforms of the initial model (blue lines), and waveforms of the final model (red lines), corresponding to the seismometers in the top-left figure. In each panel, vertical (Z), eastward (E), and northward (N) components are shown.

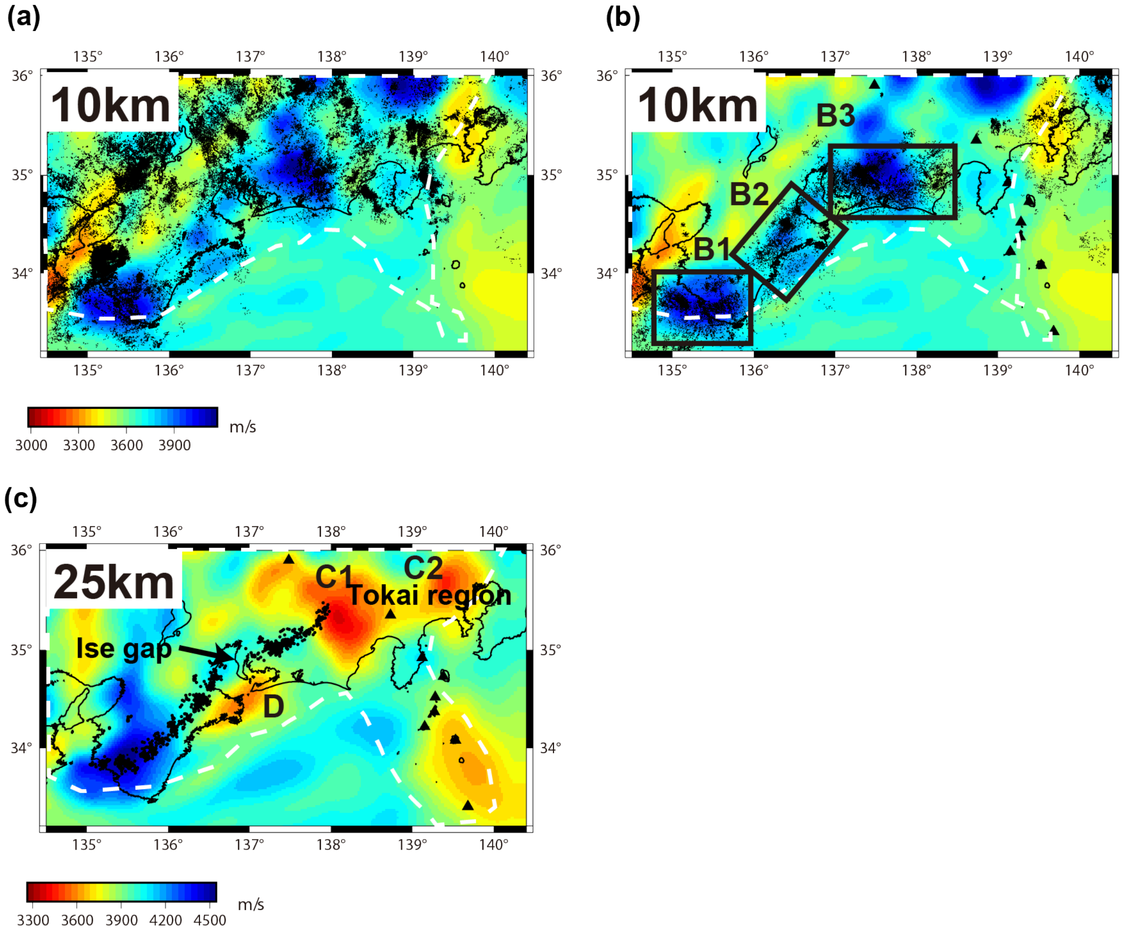

Figure 6: Zoom of S-wave velocity model. (a) S-wave velocity at 10 km depth with distributions of epicenters at depth < 25 km. (b) S-wave velocity at 10 km depth with distributions of epicenters at depth between 25 and 50 km. (c) S-wave velocity at 20 km depth with distributions of low-frequency earthquakes. White dashed lines are same as black dashed lines in figures 3. The distributions of epicenters of panel(a) and (b) were taken from Yano et al. (2017). The locations of low-frequency earthquakes were estimated by Kato et al. (2020).

319

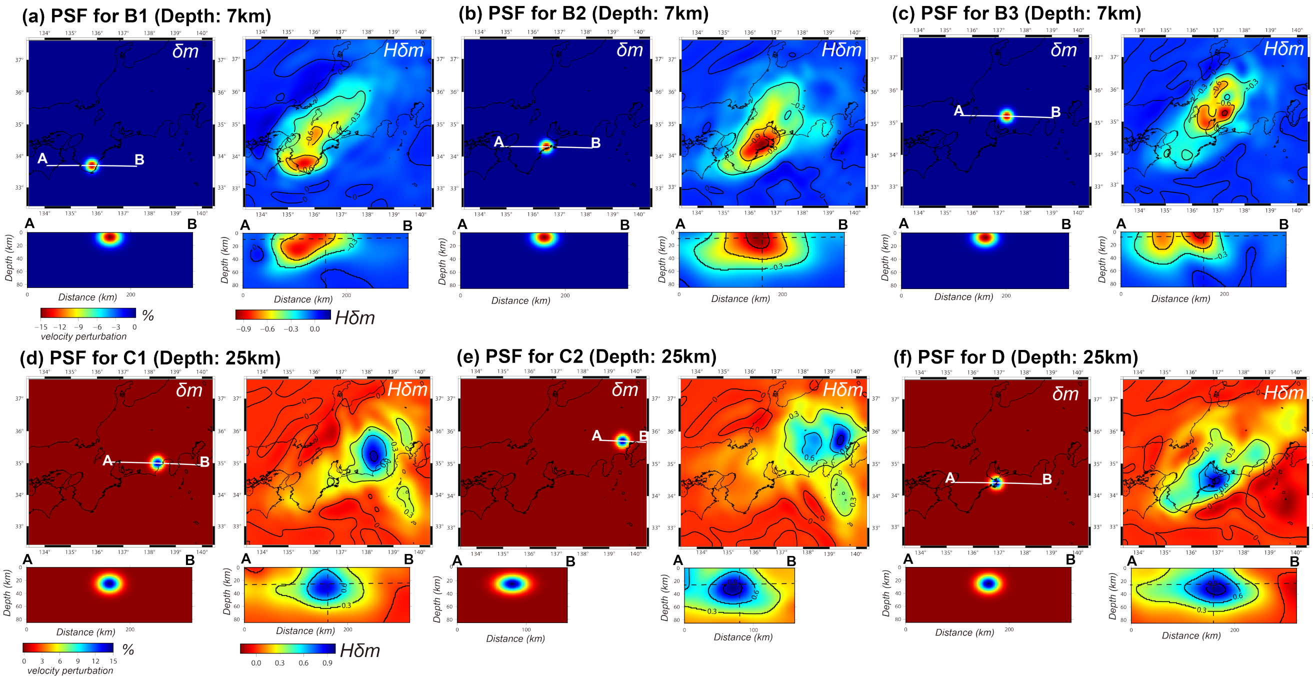

320

Figure 7: Results of PSFs test using 3D Gaussian functions. At each panel, upper two figures are horizontal sliced images and below two figures are vertical section of white line AB shown in upper left subfigure. The perturbations from final model are shown in percentage for δm and the responses $H\delta m$ are normalized.

321

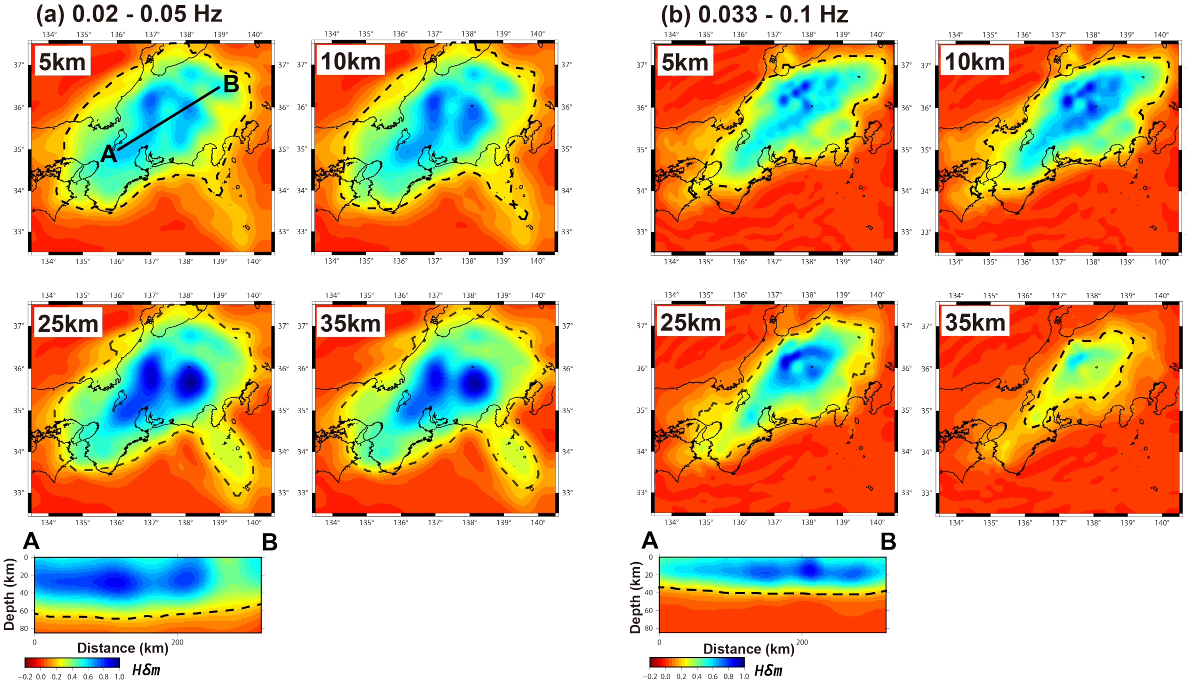

Figure 8: Results of PSFs test using constant volumetric velocity perturbation. (a) Normalized $H\delta m$ for lower frequency range 0.02-0.05 Hz. Horizontal sliced $H\delta m$ are shown in upper 4 subfigures and vertical section of black line AB is shown in bottom subfigure. The values of regions enclosed by black dashed lines are > 0.2. (b) This panel is same as panel (a), but shows the results for higher frequency range 0.033-0.1 Hz.

322

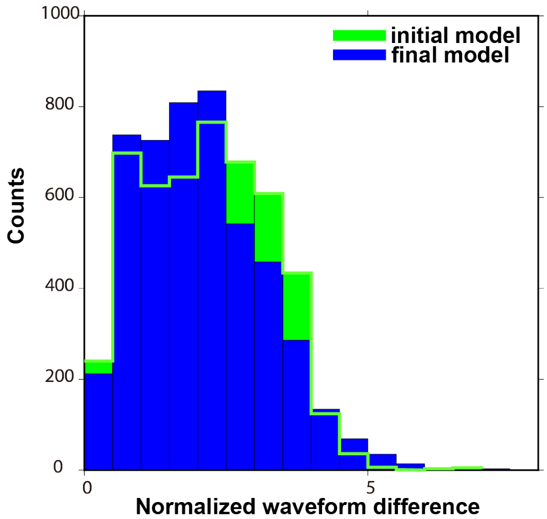

Figure 9: Normalized waveform difference of initial and final model for validation dataset.